Letter

Flow reversal triggers discontinuous shear thickening response across an erodible granular bed in a Couette-Poiseuille-like flow

Keng-Lin Lee and Fu-Ling Yang*

Department of Mechanical Engineering, National Taiwan University, Taipei 10617, Taiwan

(Received 8 November 2021; accepted 5 May 2022; published 26 May 2022)

Granular rheology is experimentally investigated in a vertical Couette-Poiseuille-like channel flow of photoelastic disks, where an erodible bed is sheared intermittently by an upward-moving shear band and a gravity-induced reverse flow. The shear band conforms to the existing nonlocal Eyring-like rheology but the bed exhibits discontinuous shear thickening from the Bagnold inertial regime near the band-bed interface to the Herschel-Bulkley plastic regime near the static wall. This newly discovered bed rheology is rate dependent and is associated with the fragility of the contact networks indicated by the statistics of local stress states inferred from the material photoelastic responses.

DOI: 10.1103/PhysRevE.105.L052901

When a granular material is sheared, shear often localizes within a narrow band of 5 to 10 grains-diameter next to an erodible bed of packed grains [1]. Understanding such shear banding is important to unifying granular rheology across flowing and static regimes for industrial and geophysical applications. Conventionally, shear banding in granular flow is analogous to a continuous liquid-solid phase transition: A liquidlike shear flow forms at where the material yields, while the adjacent solidlike bed inhibits shear motion [2,3].

However, a closer examination suggests that an erodible granular bed is not solid-rigid but fragile: The contact network therein is marginally stable so that small mechanical disturbances can lead to structural rearrangements [4–7]. Under continuous forward shearing, an erodible bed can creep with intermittent and random grain motions triggered by the adjacent flow noises, yielding exponentially decaying profiles of flow velocity and shear rate into the bed. Such flow features have been observed in Couette flows [8–10], rotating drum flows [11], Poiseuille-like channel flows [12,13], split-bottom flows [14], and wall-confined surface flows [4,5]. Several nonlocal models have been proposed to capture the creep flow dynamics based on diffusive grain cooperative mechanisms [15–19]. Yet the bed rheology may be subtler. Due to the marginally stable nature, a fragile contact network is highly anisotropic along a single direction [20], so it can be easily unjammed by applying reverse strain [21–23]. How the effect of shear reversal may enrich flow response across the erodible bed in granular shear banding flows remains to be understood.

In this Letter, we developed a vertical Couette-Poiseuille-like channel flow of photoelastic disks to study the reverse shearing effect on the rheology of erodible granular beds. An upward-moving lateral wall was imposed to drive a wall shear band next to a bed of disks which intermittently collapsed under gravity to generate reverse shearing within the material. The shear band flow conforms to the nonlocal rheology but, surprisingly, the bed exhibits a discontinuous-shear-thickening spatial transition from the Bagnold inertial to the Herschel-Bulkley plastic regime, a newly discovered fragility phenomenon for the bed rheology. We exploited photoelasticity to study local stress statistics and suggest new micromechanisms for the shear-thickening behavior in the bed.

The experimental set-up is shown in Fig. 1(a). The vertical flow channel was made of two glass plates of height $H = 70$ cm and width $W = 11$ cm kept at a narrow clearance of 3.3 mm by thin aluminum padding bars. Bidisperse disks of diameter 7 and 5 mm were cut from photoelastic sheets (Vishay PS4, Youngs modulus 4 MPa) of thickness 3.05 mm into equal amounts, giving a mean disk diameter $D = 6$ mm. The disk density $\rho = 1139\ \mathrm{kg/m^3}$ was measured. Rubber toothed belts (semicircular profile with height and spacing of $D/2$) were installed at the left and right boundary walls. The left belt was driven upward by a step motor-pulley system at a constant speed V_0 while the right belt was fixed to create a static rough wall. The belt speed was controlled to give a range of the scaled wall speed $V_0^* \equiv V_0/\sqrt{gD} = 5.53 \times 10^{-2}$–$1.05 \times 10^0$, corresponding to a system inertial number, $I_{\mathrm{sys}} \equiv V_0 D/\sqrt{gW^3} = 7.7 \times 10^{-5}$–$1.5 \times 10^{-3}$, in the quasistatic regime [24,25]. A LED light panel was placed behind the flow channel for illumination. A pair of circular polarizers were placed in front of and behind the channel to visualize the stress-induced photoelastic fringe patterns [26]. A high-speed camera (PCO.dimax HS) was focused at the channel midheight to create a square observation window of 18.4D-sidelength (the red-dashed frame) to minimize boundary effects. The camera shutter speed was set to satisfy frames per second $\simeq 10V_0/D$ to capture approximately 10 images per moving-wall displacement of D. For each V_0^*, the system was run for 2 h, and then 45 000 consecutive images were recorded for analysis.

Setting a Cartesian reference frame at the left moving wall ($x = 0$), we employed the circular Hough transform method to locate disks in each image and traced their displacements in consecutive time step to calculate individual disk velocities

*fulingyang@ntu.edu.tw

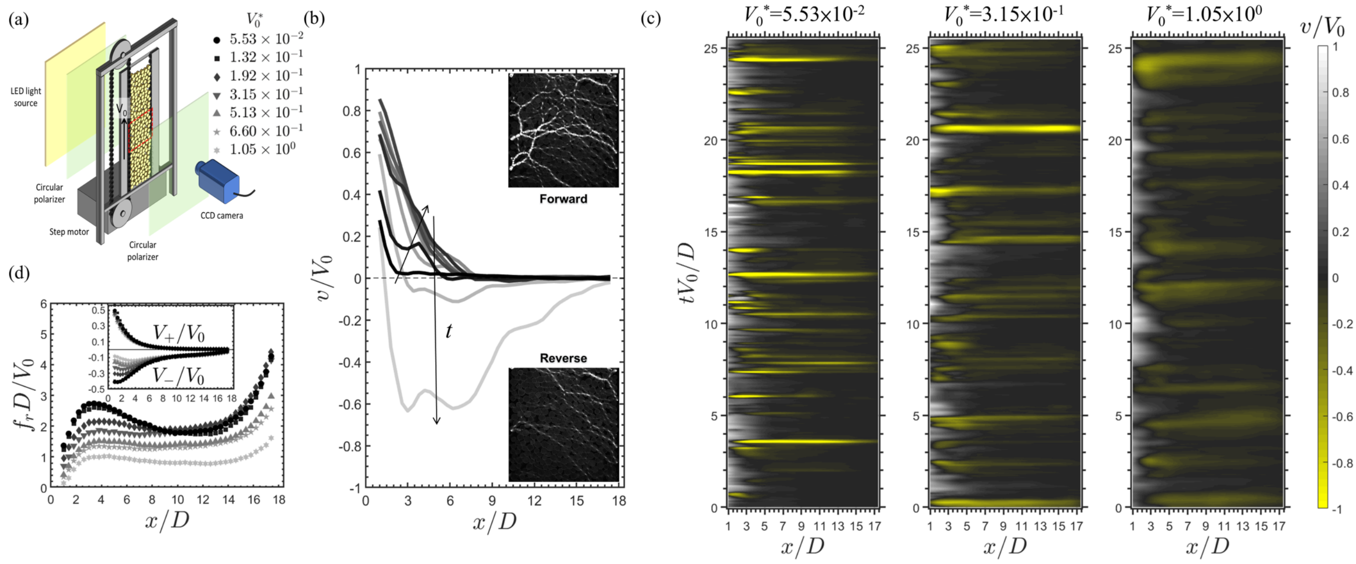

FIG. 1. (a) Experimental set-up marking the region of interest. (b) Typical evolution of instantaneous vertical velocity profiles $v(x, t)$ during a flow reversal process at $V_0^* = 5.53 \times 10^{-2}$. Top and bottom insets: Instantaneous photoelastic image before and after the contact network rearranged during the reversal. (c) Spatiotemporal diagrams for $v(x, t)$. (d) Scaled flow reversal frequency profiles under different V_0^*. Inset: Scaled mean FF (V_+) and RF (V_-) velocity profiles.

by the forward-difference scheme. We defined a retangular coarse-graining region of height $18D$ and width $2D$ to average the vertical velocities of the enclosed disks and then horizontally shifted the region by $0.4D$ to produce the instantaneous flow velocity profile $v(x, t)$. Figure 1(b) shows the time evolution of v/V_0 in one typical process of continual forward-reverse shearing as the material was dragged by the upward-moving wall and then collapsed under gravity. The upper inset displays a photoelastic snapshot during the forward shearing, showing the network of stress-bearing contacts developed over the nearly static granular bed. When the wall disturbances accumulated to some extent, the bulk collapsed and underwent reverse shearing that relaxed the network, as shown in the dimmer snapshot in the lower inset (see also the supplemental movies [27]). Such intermittent forward-reverse flow events are presented in the spatiotemporal diagrams in Fig. 1(c) for $V_0^* = 5.53 \times 10^{-2}, 3.15 \times 10^{-1}$, and 1.05×10^0.

To quantify the flow reversal intermittency, we define a forward flow (FF) state for $v(x, t) > 0$ and a reverse flow (RF) state for $v(x, t) < 0$ to count reversal transition at x when $v(x, t)$ changes from the FF (RF) to the RF (FF) state. The total number of local reversal transitions, $N_r(x)$, over the whole observation period, T, is used to evaluate a flow reversal frequency $f_r(x) = N_r(x)/T$. Figure 1(d) displays the scaled profiles of f_rD/V_0, showing that f_r is comparable with the disk rearrangement frequency at the moving wall, V_0/D, while the scaled magnitude decreases with the increase of V_0^*. In addition, we evaluated the time-averaged mean of the FF (RF) velocity, V_+ (V_-), in the inset of Fig. 1(d), showing a collapsed V_+/V_0 trend, but the magnitude of V_-/V_0 decreases as V_0^* is increased. The diminishing of the scaled f_r and V_- indicates a more continuous flow at a higher driving speed, due presumably to a stronger inertial effect on weakening the contact networks.

By averaging v at each x for all times, we obtained the steady-state velocity profiles $V(x)$ scaled by V_0 in Fig. 2(a). For each V_0^*, V/V_0 displays a thin upward flow layer for $0 < x \lesssim 3D$ and a wide downward flow segment over $3D \lesssim x < W$. Figure 2(b) focuses on the downward velocity profiles, showing clear rate dependence of the profile curvature on V_0^*. To capture the velocity curvature, we computed the local shear rate $\dot{\gamma}(x) \equiv dV/dx$ using the central difference scheme and normalized it with V_0/D. Figure 2(c) shows the segment of negative $\dot{\gamma}$ next to the moving wall, where its magnitude decays monotonically with x and vanishes around $x \approx 6D$. Then $\dot{\gamma}$ flips the sign and grows toward the static wall with much smaller magnitudes [Fig. 2(d)]. We identify the negative-$\dot{\gamma}$ segment as a shear band and the much weaker but wider positive-$\dot{\gamma}$ segment as a slowly deforming granular bed. The shear band width, evaluated at the band-bed interface, $x = \delta_i$ where $\dot{\gamma} = 0$, grows from around $5.5D$ to $7D$ when V_0^* is increased [Fig. 2(e)]. We observe that $\dot{\gamma}$ in the bed also decays monotonically over a similar distance of $6D$ from the static wall but, surprisingly, saturates to a plateau in the core and drops sharply to zero at the interface. The span of the shear-rate plateau and its normalized magnitude decrease with the increase of V_0^*. This rate-dependent shear-rate plateau phenomenon is distinct from the commonly reported quasistatic shear band dynamics for which the shear rate asymptotically vanishes from a flow source and the profile shape is independent of the flow rate [5,6,9,10,12,13].

Some may associate this shear-rate plateau with the core plug of two-dimensional (2D) Poiseuille-like granular channel flows [12,28] in which the core region exhibits a solid fraction ϕ above the value of 2D random close packing, $\phi_{\rm rcp} \approx 0.84$, to inhibit shear motion. We estimated the steady-state solid fraction, $\phi(x)$, by averaging the portion of the total disk area in each coarse-graining region over all t in Fig. 2(f). It shows that ϕ over the shear-rate plateau is higher than the values in the shear band and near the static wall but below $\phi_{\rm rcp}$. When V_0^* is increased, an increase in the plateau's ϕ is observed, associated with the

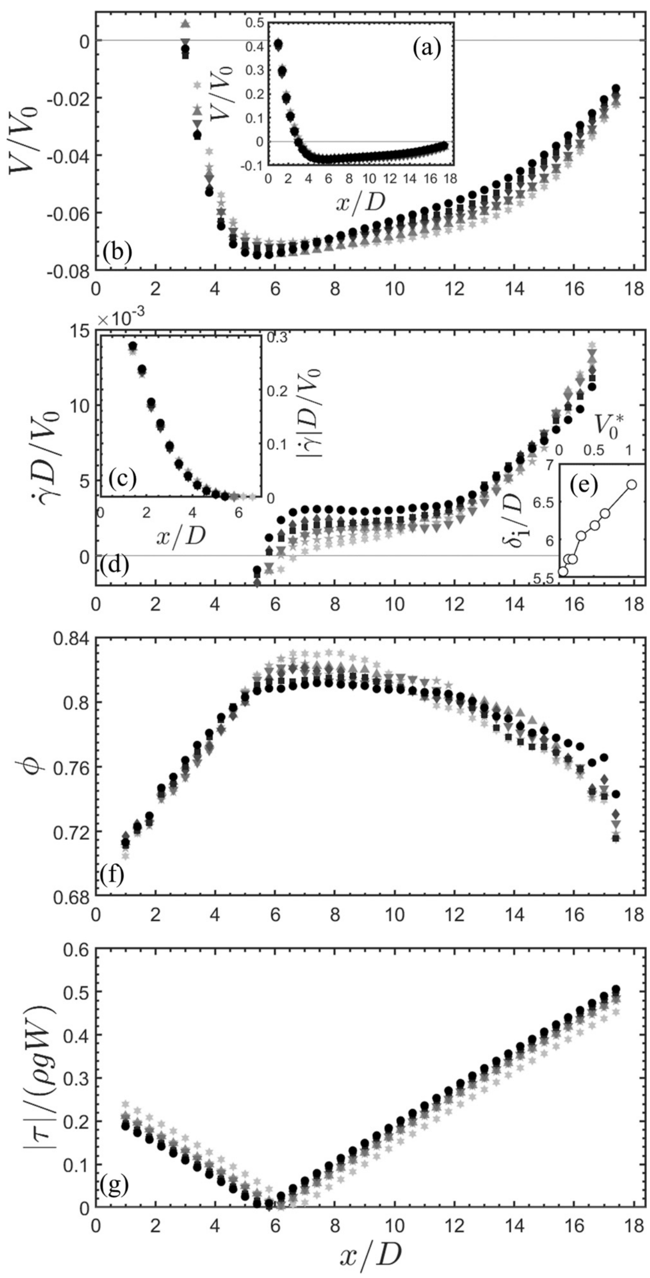

FIG. 2. (a) Time-averaged scaled velocity profiles, where the downward flow segments are enlarged in (b); [(c) and (d)] scaled shear rate profiles within the shear band and the bed, respectively; (e) scaled shear band widths versus V_0^*; (f) solid fraction profiles; and (g) scaled shear stress profiles. The symbols correspond to different V_0^* given in Fig. 1(a).

diminishing of the scaled shear-rate plateau magnitude in Fig. 2(d).

To study the flow rheology, we evaluated the local shear stress τ by integrating the steady momentum balance equation in the vertical direction y, $\partial_x\tau = -\rho\phi(x)g$, subject to a shear-free condition $\tau = 0$ at the interface $x = \delta_{\rm i}$ (where $\dot{\gamma} = 0$). Note that the gradient of normal stress along y in this momentum balance is examined to be negligible due to the large height-to-width aspect ratio (see the details in supplementary material [27]), as in other channel flow analysis [12]. Figure 2(g) shows $|\tau|$ appears linear in x for all V_0^*, indicating a negligible influence of the spatial variation of ϕ on τ. Figure 3(a) plots $|\tau|$ versus the corresponding $|\dot{\gamma}|$ over the shear band ($0 < x < \delta_{\rm i}$), displaying a pseudoplastic behavior (shear-thinning, $|d\tau/d\dot{\gamma}| < 1$) for all V_0^*. The data can be nicely fitted to

$$|\dot{\gamma}| = \frac{aV_0}{D}\left[\exp\left(-\frac{\tau_{\rm c} - |\tau|}{\delta\tau(x)}\right) - \exp\left(-\frac{\tau_{\rm c} + |\tau|}{\delta\tau(x)}\right)\right], \quad (1)$$

if we follow the nonlocal rheology to understand the shear-band plastic behavior as the result of an Erying-like stress-activation process [12,16,17,29,30]. Here aV_0/D represents an attempt frequency, and $\tau_c = |\tau(x_{\rm mw})|$ is a critical yield stress characterized by the moving-wall shear stress with $x_{\rm mw} = 1.2D$. The first (second) exponential term describes a Boltzmann-like probability of a forward (backward) shear event as a stress barrier $\tau_c - |\tau|$ ($\tau_c + |\tau|$) is overcome by stress fluctuations $\delta\tau$ generated from the yielded wall region. We propose $\delta\tau(x) = b\tau_c \exp[-(x - x_{\rm mw})/l]$ by assuming the fluctuation strength scales with the yield stress and decays exponentially from the yielded region. How Eq. (1) is manipulated to fit the $|\tau| - |\dot{\gamma}|$ data is given in Supplemental Material [27]. The insets of Fig. 3(a) show the fit parameters $a \approx 0.28$, $b \approx 0.4$, and the decay length $l \approx 5.5D$ which are independent of V_0^*. The satisfactory data fit demonstrates that the Eyring activation process underlies the shear-band rheology, suggesting an *Eyring-like plastic* regime.

By contrast, the data in the bed region ($\delta_{\rm i} < x < W$) unveil three distinct flow regimes [Fig. 3(b)]. Near the band-bed interface, the flow is Bagnold, $\tau = A_{\rm Bag}\dot{\gamma}^2$ (the dashed lines), characterizing a grain-inertia-dominated flow process in an *inertial* regime [31–35]. The coefficient $A_{\rm Bag}$ decreases by an order of magnitude with V_0^* [Fig. 3(c)]. Near the static wall, the data, however, show a power-law relation, $\tau = A_P\dot{\gamma}^\alpha$ (the solid lines), with α decreasing slightly from 0.5 to 0.35 and A_P from 8 to 6 with the increase of V_0^* [Fig. 3(c)]. This behavior corresponds to the Herschel-Bulkley plastic rheology at large shear limit, giving a *HB plastic* regime [33–35].

Intriguingly, the Bagnold inertial regime is bridged to the HB plastic regime through a noticeable jump of τ at a critical $\dot{\gamma}$, corresponding to the plateau value in Fig. 2(d). The flow curve resembles the discontinuous shear thickening (DST) in dense suspensions and other dry granular systems [34,36–40]. In continuous forward shearing, DST results from the sudden formation of persistent contact networks when the system is loaded above an onset stress at which enduring frictional contacts span the system [37–42]. However, DST in our system may result from different contact network dynamics in the presence of reverse shearing. As illustrated in Fig. 1(b), reverse shearing continually relaxes stress-bearing contacts around the shear band, yielding a doward inertial flow under gravity to erode the bed. Yet the inertial erosion is concurrently suppressed by the remaining contact networks that stand persistently from the static wall. The encounter between the liquidlike and solidlike responses hence causes shear to thicken into the bed. This thickening phenomenon provides a direct rheological evidence of a fragile erodible bed in which an unjammed and a jammed state can coexist, echoing the result of strain-controlled shear tests [21,22].

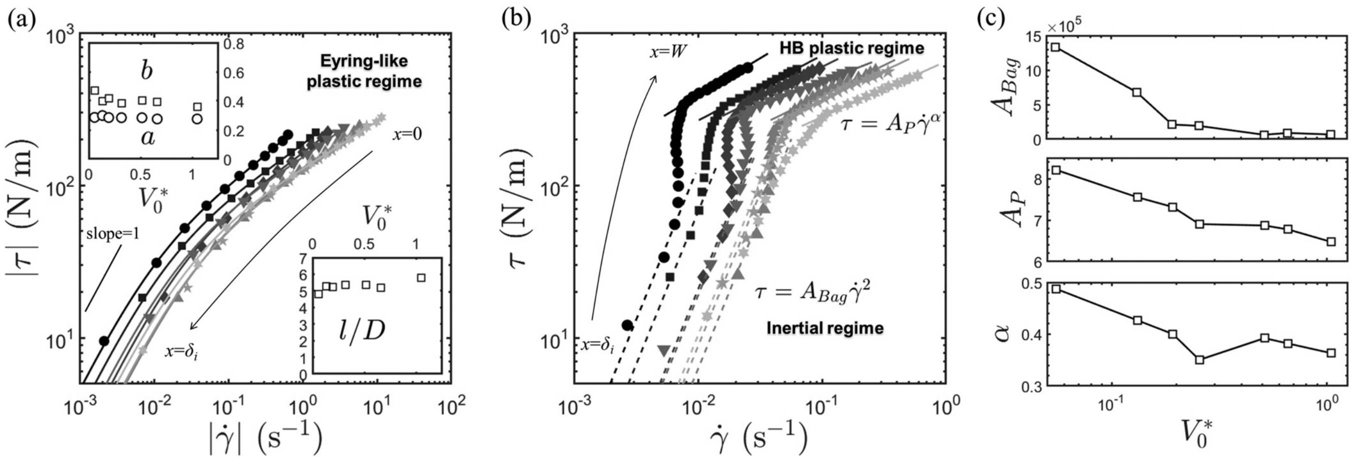

FIG. 3. Rheological relations for shear stress τ versus shear rate $\dot{\gamma}$ in (a) the shear band ($0 < x < \delta_i$) and (b) the bed ($\delta_i < x < W$). Solid lines in (a): the Eyring model in Eq. (1) with the fitting parameters given in the insets. (c) The fitting parameters for the Bagnold and the HB model shown in (b).

With the aid of fitting to the aforementioned τ-$\dot{\gamma}$ relations, we identified the span of each flow regime under different V_0^* to construct a flow-regime map in Fig. 4. Although the two wall plastic regimes appear comparable in size ($\approx 6D$) for all V_0^*, the rise of V_0^* causes the inertial regime to expand but the DST regime to shrink noticeably. Interestingly, at the highest $V_0^* = 1.05$, the DST regime nearly vanishes so that the inertial and the plastic regimes bridge smoothly, featuring continuous shear thickening (CST) [see also Fig. 3(b)], similarly to the flow curves reported in volume-controlled homogeneous shearing systems [33,35]. We speculate that the DST-CST transition arises from a collision-induced slippage effect [43–45]: Increasing the driving speed creates significant collisional noises to activate slip events at persistent contacts developed from the static wall, weakening the dramatic shear thickening in the intermediate region. This speculation is supported by the core compaction in Fig. 2(f), indicating that the bed disks near the band can slip past one another more easily at higher V_0^* to explore denser configurations, resembling bulk compaction at high shear rates in rheometer experiments [43,44]. The slippage mechanism can also account for the significant drop in A_{Bag} with V_0^* [Fig. 3(c)] as more slip events in a faster flow weaken the ability of inertial disk motion to transport momentum.

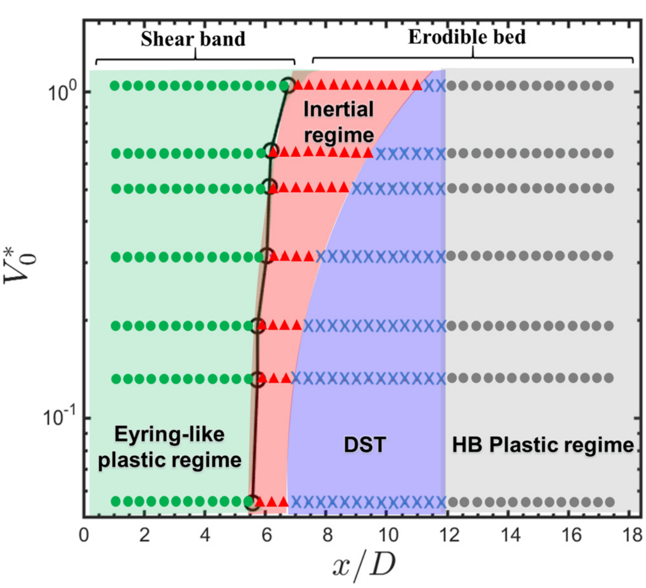

FIG. 4. Flow-regime map. The open circles threaded by the solid line presents the shear-band width data in Fig. 2(e).

To provide more insights into the rheological response, we study the local stress statistics by exploiting the photoelastic images to compute a gradient-square parameter $G^2(x,t) = \sum(\nabla I)^2$ to infer instantaneous local stress magnitude [8,26]. Here ∇I is the pixelwise gradient of the light intensity field at t [8,26], and the sum is made over the coarse-graining region centered at x. We evaluate the local probability distribution function, $P(f)$, for a normalized stress parameter $f = G^2/\langle G^2\rangle$, where $\langle G^2\rangle$ is the mean of G^2 over all x and t. Figure 5 shows $P(f)$ for (a) $V_0^* = 5.53 \times 10^{-2}$ and (b) 6.6×10^{-1}, where $\delta_{I\text{-DST}}$ and $\delta_{\text{DST-}P}$ denote the boundaries between the three regimes and $x_{\mathrm{sw}} = 17.4D$ is the data location closest to the static wall. Intriguingly, the cross-flow $P(f)$ intersect nicely at $f = 1$, separating the local stress into strong ($f > 1$) and weak ($f < 1$) states. For strong stress, $P(f)$

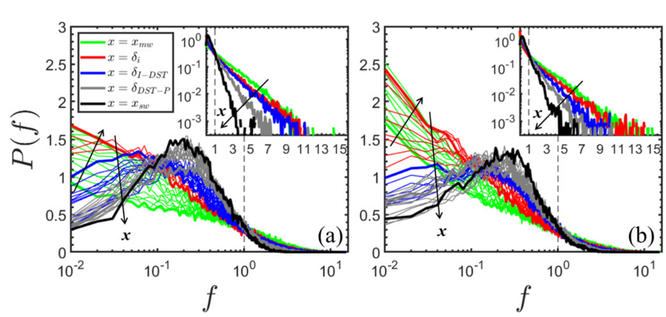

FIG. 5. Probability distribution functions of the normalized stress state $P(f)$ across the flow for (a) $V_0^* = 5.53 \times 10^{-2}$ and (b) $V_0^* = 6.6 \times 10^{-1}$. $P(f)$ on the walls and the flow regime boundaries are marked by thick colored lines while the thin lines denote $P(f)$ within the flow regimes. The insets show $P(f)$ in the strong-stress state ($f > 1$).

decays nearly exponentially with f, with the decay breadth diminishing from the moving to the static wall. The broad $P(f)$ near the moving wall indicates large stress fluctuations as the material yields under forward shearing. The spatially diminishing decay breadth further supports the proposed $\delta\tau(x)$ trend in the Erying model (1).

The shape of $P(f)$ for weak stress states ($f < 1$), however, varies in a complex way across the flow regimes. Within the shear band (green lines, $0 < x < \delta_i$), $P(f)$ grows logarithmically as f tends to zero, and the slope steepens near the band-bed interface (thick red line, $x = \delta_i$). This shape feature clearly demonstrates a fragile mechanical response that, during the reverse shearing, stress-bearing contacts around the band region are dramatically relaxed, especially close to the interface where contacts are too far to be effectively rejuvenated by the subsequent wall shearing. Across the inertial regime (thin red lines, $\delta_i < x < \delta_{I\text{-DST}}$), $P(f)$ decreases and flattens at vanishing f. The flattening reflects a small but growing stress contribution when the inertial flow shears and erodes the bed. As entering the DST regime (blues lines, $\delta_{I\text{-DST}} < x < \delta_{\text{DST-}P}$), $P(f)$ is peaked at a finite f which grows as approaching closer to the HB plastic regime (gray lines, $x > \delta_{\text{DST-}P}$). Such a peak characteristic reflects a certain portion of stresses resulting from persistent contact networks that stand on the static wall for much longer periods than the wall shearing time, as inferred previously from the rheological result [also visualized in the lower photoealstic images in Fig. 1(b)].

At the higher V_0^* in Fig. 5(b), $P(f)$ across the shear band and the inertial regime ($0 < x \lesssim \delta_{I\text{-DST}}$) broadens and develops higher values at weak stress states. This result supports our earlier argument that enhancing wall shearing yields stronger collision-induced fluctuations to weaken the persistent contact networks and hence to result in the DST-CST transition.

To conclude, this work presents a Couette-Poiseuille-like granular flow experiment in which intermittent shear reversal developed across a wall shear band and the adjacent erodible bed. While the nonlocal Eyring-like model [Eq. (1)] can capture the rheological response in the shear band, the bed exhibits a complex rate-dependent shear-thickening behavior due to the fragility of the contact networks. This is surprisingly in contrast to the rate-independent creeping bed behavior in continuous forward shearing flows, suggesting that the unique shear reversal generates an internal fluidization process other than boundary shearing. As this internal process introduces new time and length scales, the nonlocal rheology models require further investigation.

The financial support from the Ministry of Science and Technology of Taiwan (109-2628-E-002-002-MY3 and 110-2923-E-002-003) is acknowledged.

[1] P. Schall and M. van Hecke, Annu. Rev. Fluid Mech. **42**, 67 (2010).
[2] P. Jop, Y. Forterre, and O. Pouliquen, J. Fluid Mech. **541**, 167 (2005).
[3] P.-Y. Lagre, L. Staron, and S. Popinet, J. Fluid Mech. **686**, 378 (2011).
[4] T. S. Komatsu, S. Inagaki, N. Nakagawa, and S. Nasuno, Phys. Rev. Lett. **86**, 1757 (2001).
[5] P. Richard, A. Valance, J.-F. Métayer, P. Sanchez, J. Crassous, M. Louge, and R. Delannay, Phys. Rev. Lett. **101**, 248002 (2008).
[6] D. Berzi, J. T. Jenkins, and P. Richard, Soft Matter **15**, 7173 (2019).
[7] N. Deshpande, D. Furbish, P. Arratia, and D. Jerolmack, Nat. Commun. **12**, 3909 (2021).
[8] D. Howell, R. P. Behringer, and C. Veje, Phys. Rev. Lett. **82**, 5241 (1999).
[9] E. I. Corwin, H. M. Jaeger, and S. R. Nagel, Nature (Lond.) **435**, 1075 (2005).
[10] G. Koval, J.-N. Roux, A. Corfdir, and F. Chevoir, Phys. Rev. E **79**, 021306 (2009).
[11] A. V. Orpe and D. V. Khakhar, J. Fluid Mech. **571**, 1 (2007).
[12] O. Pouliquen and R. Gutfraind, Phys. Rev. E **53**, 552 (1996).
[13] K. S. Ananda, S. Moka, and P. R. Nott, J. Fluid Mech. **610**, 69 (2008).
[14] V. H. M. Fenistein, D., Nature (London) **425**, 256 (2003).
[15] J. T. Jenkins, Phys. Fluids **18**, 103307 (2006).
[16] O. Pouliquen and Y. Forterre, Philos. Trans. R. Soc. Lond. A **367**, 5091 (2009).
[17] K. Kamrin and G. Koval, Phys. Rev. Lett. **108**, 178301 (2012).
[18] M. Bouzid, M. Trulsson, P. Claudin, E. Clément, and B. Andreotti, Phys. Rev. Lett. **111**, 238301 (2013).
[19] K.-L. Lee and F.-L. Yang, Phys. Rev. E **96**, 062909 (2017).
[20] M. E. Cates, J. P. Wittmer, J.-P. Bouchaud, and P. Claudin, Phys. Rev. Lett. **81**, 1841 (1998).
[21] D. Bi, J. Zhang, B. Chakraborty, and R. P. Behringer, Nature (London) **480**, 355 (2011).
[22] Y. Zhao, J. Barés, H. Zheng, J. E. S. Socolar, and R. P. Behringer, Phys. Rev. Lett. **123**, 158001 (2019).
[23] M. Otsuki and H. Hayakawa, Phys. Rev. E **101**, 032905 (2020).
[24] GDR-Midi, Eur. Phys. J. E **14**, 341 (2004).
[25] F. da Cruz, S. Emam, M. Prochnow, J.-N. Roux, and F. Chevoir, Phys. Rev. E **72**, 021309 (2005).
[26] K. E. Daniels, J. E. Kollmer, and J. G. Puckett, Rev. Sci. Instrum. **88**, 051808 (2017).
[27] See Supplemental Material at http://link.aps.org/supplemental/10.1103/PhysRevE.105.L052901 for explaining why the vertical stress gradient can be neglected in our system and provides the procedures to complete the Eyring model fit, which includes Refs. [12,46].
[28] R. Gutfraind and O. Pouliquen, Mech. Mater. **24**, 273 (1996).
[29] K. A. Reddy, Y. Forterre, and O. Pouliquen, Phys. Rev. Lett. **106**, 108301 (2011).
[30] Q. Zhang and K. Kamrin, Phys. Rev. Lett. **118**, 058001 (2017).
[31] R. A. Bagnold, Proc. R. Soc. Lond. A **225**, 49 (1954).
[32] C. S. Campbell, Powder Technol. **162**, 208 (2006).
[33] S. Chialvo, J. Sun, and S. Sundaresan, Phys. Rev. E **85**, 021305 (2012).
[34] M. Otsuki and H. Hayakawa, Phys. Rev. E **83**, 051301 (2011).
[35] D. Vescovi and S. Luding, Soft Matter **12**, 8616 (2016).

[36] E. Brown and H. M. Jaeger, J. Rheol. **56**, 875 (2012).
[37] R. Seto, R. Mari, J. F. Morris, and M. M. Denn, Phys. Rev. Lett. **111**, 218301 (2013).
[38] M. Wyart and M. E. Cates, Phys. Rev. Lett. **112**, 098302 (2014).
[39] C. Ness and J. Sun, Soft Matter **12**, 914 (2016).
[40] S. H. E. Rahbari, M. Otsuki, and T. Pschel, Commun. Phys. **4**, 71 (2021).
[41] B. M. Guy, M. Hermes, and W. C. K. Poon, Phys. Rev. Lett. **115**, 088304 (2015).
[42] S. Saw, M. Grob, A. Zippelius, and C. Heussinger, Phys. Rev. E **101**, 012602 (2020).
[43] K. Lu, E. E. Brodsky, and H. P. Kavehpour, J. Fluid Mech. **587**, 347 (2007).
[44] N. J. van der Elst, E. E. Brodsky, P.-Y. Le Bas, and P. A. Johnson, J. Geophys. Res. **117**, B09314 (2012).
[45] E. DeGiuli and M. Wyart, Proc. Natl. Acad. Sci. USA **114**, 9284 (2017).
[46] H. A. Janssen, Z. Ver. Dtsch. Ing. **39**, 1045 (1895).